Phase-Matched Second-Harmonic Generation in an On-Chip $LiNbO_3$ Microresonator

Jintian Lin,[1] Yingxin Xu,[2] Jielei Ni,[3] Min Wang,[1,4] Zhiwei Fang,[1,5] Lingling Qiao,[1] Wei Fang,[2,*] and Ya Cheng[1,6,†]

[1]*State Key Laboratory of High Field Laser Physics, Shanghai Institute of Optics and Fine Mechanics, Chinese Academy of Sciences, Shanghai 201800, China*

[2]*State Key Laboratory of Modern Optical Instrumentation, College of Optical Science and Engineering, Zhejiang University, Hangzhou 310027, China*

[3]*Department of Electrical and Electronic Engineering, The University of Hong Kong, Pokfulam Road, Hong Kong 999077, China*

[4]*University of Chinese Academy of Sciences, Beijing 100049, China*

[5]*School of Physical Science and Technology, ShanghaiTech University, Shanghai 200031, China*

[6]*State Key Laboratory of Precision Spectroscopy, East China Normal University, Shanghai 200062, China*

(Received 11 January 2016; revised manuscript received 24 March 2016; published 1 July 2016)

The realization of an efficient nonlinear parametric process in microresonators is a challenging issue largely because of an inherent difficulty in simultaneously ensuring the phase-matching condition and a coherent multiple-resonance condition for all the waves participating in the nonlinear conversion process. Here, we demonstrate highly efficient second-harmonic generation in an on-chip $LiNbO_3$ microresonator fabricated by femtosecond-laser direct writing. We overcome the above difficulty by selectively exciting high-order modes in the fabricated thin-disk microresonator. Thanks to the low optical absorption and high nonlinear optical coefficient of $LiNbO_3$ crystal, we achieve a normalized conversion efficiency of $1.106 \times 10^{-3}/\mathrm{mW}$ in the on-chip $LiNbO_3$ microdisk with a diameter of approximately 102 μm.

DOI: 10.1103/PhysRevApplied.6.014002

I. INTRODUCTION

Nonlinear optical processes in whispering-gallery-mode (WGM) microresonators attract much attention. Because of the strong confinement of light in a small volume, a WGM microresonator can dramatically boost the strength of the light field, thereby promoting the nonlinear interaction between the light and the resonator material. Today, the widely adopted approaches to fabricate high-quality (high-Q) WGM microresonators on semiconductor or dielectric chips are based on defining circular pads using a lithographic method followed by the formation of the microresonators via dry or wet etching [1–3]. In combination with CO_2 laser surface reflow, ultra-high-Q factors on the order of approximately 10^8 have been demonstrated in silica microtoroid resonators which have benefited applications ranging from nonlinear optics and high-sensitivity biosensing to cavity quantum electrodynamics and optomechanics [3–5]. In comparison with glass materials, crystals can have higher nonlinear coefficients, a broader transmission window, and a higher damage threshold under exposure of intense light fields [6], making the crystalline microresonators particularly attractive for nonlinear optics and quantum light-source applications [7–15].

It is worth mentioning that in the nonlinear frequency-conversion processes, phase matching often plays a determining role in terms of the achievable conversion efficiency [16,17]. Phase matching in bulk materials is typically realized using either critical phase matching (CPM) by arranging the angular crystal orientation with respect to the propagation direction of the incident light or quasi-phase matching (QPM) by patterning the optical nonlinearity of materials [17,18]. However, in general, it is not straightforward to achieve perfect CPM in a WGM microresonator because of the fact that when the waves circulate around the periphery of the microresonator, they can experience varying crystal orientation. The QPM is compatible with the nonlinear frequency conversion in WGM microresonators, which has indeed been demonstrated [19]. Nevertheless, to make use of the QPM mechanism, the additional nonlinearity patterning on crystalline microresonators leads to increased complexity, particularly for microresonators of small sizes except for the crystals of $\overline{4}$ symmetry [19]. Recently, Lin *et al.* [20] proposed a different phase-matching scheme for second-harmonic generation (SHG) in a WGM resonator fabricated by mechanical polishing. The scheme is coined as cyclic semiphase matching (CSPM). In the CSPM, perfect phase matching takes place cyclically at four azimuth angles where the ideal angular configurations of the crystal and the propagating beams exist. The implementation of CSPM in a large WGM resonator is relatively easy for its high mode density, thereby facilitating both the fundamental and second-harmonic waves to be tuned on resonance simultaneously. Here, we demonstrate that the CSPM can also be employed for phase-matched SHG in an on-chip $LiNbO_3$

*wfang08@zju.edu.cn
†ya.cheng@siom.ac.cn

 © 2016 American Physical Society

microresonator with a diameter of approximately 100 μm. It should be stressed that for high-Q microresonators of small sizes, maintaining the coherent double-resonance condition in the phase-matched SHG is extremely challenging because of the sparse frequency distributions of the high-Q modes for both the fundamental and second-harmonic waves. We overcome the difficulty by controlling the geometrical dimensions of the $LiNbO_3$ microdisk and selectively exciting a certain high-order mode of the fundamental wave in the microresonator.

II. EXPERIMENT

Phase-matched SHG is carried out in an X-cut $LiNbO_3$ microresonator using an experimental setup as schematically shown in Fig. 1. In our experiment, commercially available ion-sliced X-cut $LiNbO_3$ thin film with a thicknesses of 0.709 μm (NANOLN, Jinan Jingzheng Electronics Co., Ltd) is chosen for fabricating the $LiNbO_3$ microdisk resonator. As the $LiNbO_3$ film cannot be efficiently processed by wet or dry etching, femtosecond-laser direct writing followed by focused-ion-beam (FIB) milling and selective chemical wet etching is used to form a free-standing high-Q $LiNbO_3$ microdisk suspended on a silica pedestal. Details of the process flow of fabrication of the $LiNbO_3$ microresonator are described in Refs. [10,11]. The $LiNbO_3$ microresonator fabricated on an X-cut $LiNbO_3$ thin film has a thickness of 709 nm and a diameter of approximately 102.3 μm, as shown by its scanning-electron-microscope (SEM) image in the right-hand-side inset of Fig. 1. The optical axis of the crystal lies in the plane of the $LiNbO_3$ microdisk.

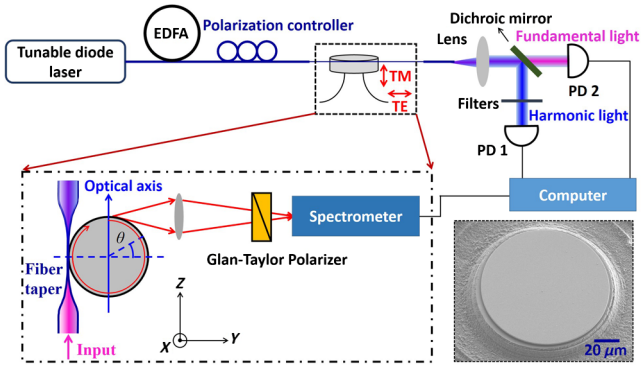

FIG. 1. Experimental setup for the SHG in the $LiNbO_3$ microresonator. Polarization states of TE and TM are schematically illustrated near the microresonator. The pump and second-harmonic signals coupled out of the microresonator with the fiber taper are collimated by an objective lens with a NA of 0.25. The inset on the left-hand side is the experimental setup of determining the polarization states of the light beams scattering from the edge of the microresonator, where θ is the angle between the wave vector and optical axis of the crystal; the inset on the right-hand side is a SEM image of the microresonator.

The second harmonic is generated using a continuous-wave tunable diode laser (New Focus, Model 688-LN) amplified by an erbium-ytterbium-doped fiber amplifier as the pump source. The diode laser has a linewidth of 10 MHz and a spectral tuning range from 1535 to 1570 nm. A fiber taper placed in contact with the top surface (Y-Z plane) of the microdisk is used for coupling the pump light into the $LiNbO_3$ microresonator, which is fabricated by pulling a section of SMF-28 fiber to a diameter of 700 nm. We choose a relatively large thickness based on our simulation as described below; therefore, the microresonator can support high-order axial modes to fulfill the double-resonant condition. The same fiber taper is also used for coupling the second harmonic out of the $LiNbO_3$ microresonator. Selective excitation of a certain spatial mode can be achieved by adjusting the position of the fiber taper with respect to the microresonator, which is controlled by an XYZ-piezo stage. By using an online fiber polarization controller, the polarization of the pump laser can be chosen to enable excitation of the TM (transverse magnetic) mode in the microdisk; i.e., the polarization of the pump light in the microresonator is perpendicular to the disk plane. The signals from the output port of the fiber taper are collimated by an objective lens with a numerical aperture (NA) of 0.25 and separated from the pump light by a dichroic mirror. The generated second-harmonic signal is measured with a photodetector (PD, PD 1 in Fig. 1). Meanwhile, the pump light passing through the dichroic mirror is measured with another PD (PD 2 in Fig. 1).

We use a Glan-Taylor polarizer to examine the polarization states of fundamental and second-harmonic waves in the microresonator in free space. A 10× objective lens with a NA of 0.25 is used to collect the scattering light from the microresonator. The spectra of scattered fundamental and second-harmonic waves are measured by the spectrometer (Andor, Model Du920) after passing through a calibrated Glan-Taylor polarizer, as illustrated in the left-hand-side inset of Fig. 1. An InGaAs detector is employed for detecting the scattered fundamental light at approximately 1540 nm. To detect the generated second-harmonic wave at approximately 770 nm, a charge-coupled-device (CCD) array detector is used instead.

III. DEMONSTRATION OF EFFICIENT SHG UNDER THE DOUBLE-RESONANCE CONDITION

Figure 2(a) shows the measured spectrum of the second-harmonic signal at a wavelength λ_{SH} of 770.065 nm, which is obtained with a pump light whose spectrum is presented in Fig. 2(b) for comparison. The wavelength λ_F of the pump light is 1540.13 nm, which is exactly twice that of the second-harmonic signal. We notice that under this condition, the second-harmonic beam is TE (transverse electric) polarized, whereas the fundamental beam is TM polarized. As shown by the optical micrograph captured by a CCD camera in Fig. 2(c), the scattering light of the

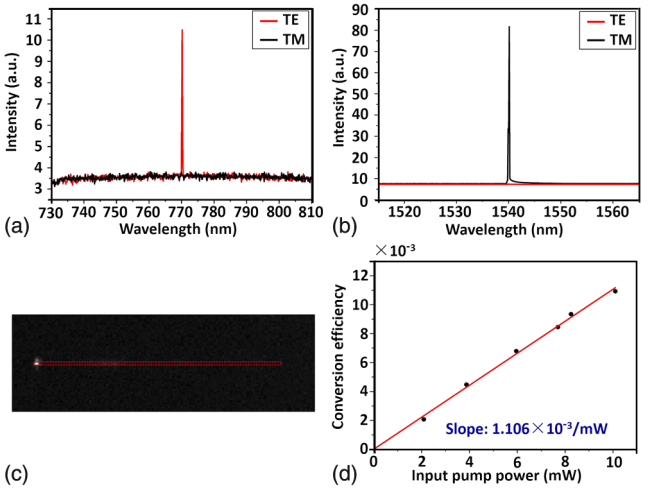

FIG. 2. (a) The spectrum of the TE-polarized second harmonic generated from the microresonator. (b) The spectrum of the TM-polarized pump light. (c) Side-view optical micrograph of the second-harmonic scattering from the edge of the microresonator, where the red rectangle depicts the contour of the microdisk. (d) The SHG conversion efficiency plotted as a function of the pump power.

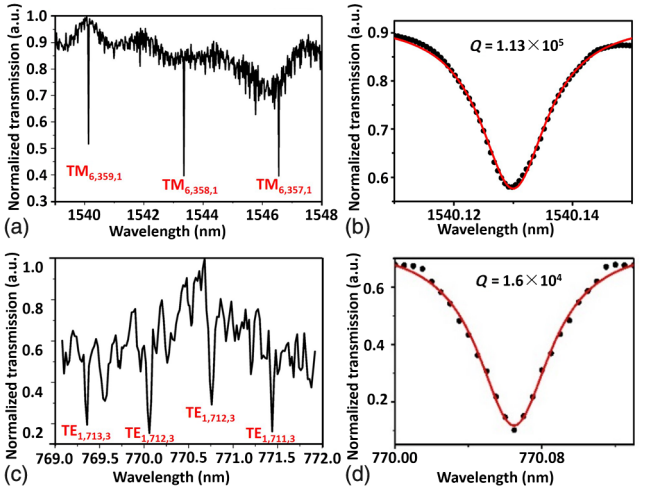

FIG. 3. (a) Transmission spectrum around 1540 nm recorded by coupling the fiber taper with the microresonator. (b) Lorentzian fit (red line) of measured spectrum around the resonant wavelength at 1540.13 nm (black line), showing a Q factor of 1.13×10^5. (c) Transmission spectrum around 770 nm recorded by coupling the fiber taper with the microresonator. (d) Lorentzian fit (red solid line) of measured spectrum around the resonant wavelength at 770.065 nm (black dotted line), showing a Q factor of 1.6×10^4.

second harmonic is clearly visible on the edge of the microdisk, which is the nature of WGM propagation. We further measure the conversion efficiency of SHG as a function of the input laser power. Here, the conversion efficiency is estimated based on the powers of SHG signal collected from the fiber output and the fundamental light input into the fiber. Actually, the conversion efficiency should be higher in the device if all the propagation losses and coupling efficiencies are taken into account. Experimentally, the power of the pump laser is first measured before it is coupled into the microresonator at the input port of the fiber taper, whereas the power of the second harmonic is measured from the output port of the fiber taper after removing the fundamental light with a dichroic mirror followed by three pieces of short-pass filters. The transmission of the short-pass filter at approximately 1540-nm wavelength is 0.08%, whereas the transmission at approximately 770-nm wavelength is 99%. We observe that the conversion efficiency increases linearly with the increasing input laser power. From the slope of the fitting line in Fig. 2(d), a normalized conversion efficiency of $1.106 \times 10^{-3}/\mathrm{mW}$ can be determined. The result indicates that the combination of the high-Q $LiNbO_3$ microresonator and the CSPM mechanism can provide promising potential for highly efficient nonlinear wavelength conversion [20].

It is instructive to clarify whether the fundamental and second-harmonic waves both satisfy the resonance condition in our experiment, which is confirmed by the transmission spectra measured around the wavelengths of fundamental TM and second-harmonic TE waves as shown in Figs. 3(a) and 3(c), respectively. Indeed, from the spectra, we confirm that both the fundamental and second-harmonic wavelengths are on resonance with the modes in the $LiNbO_3$ microdisk. It is noteworthy that the relative "messy" spectrum at 770 nm is mainly because of the existence of much denser modes in this wavelength region, including high-order axial modes. One can also evaluate the Q factors based on the spectra. At the pump wavelength around 1540.13 nm, the measured Q factor reaches 1.13×10^5 [see Fig. 3(b)]. Around the spectral range of the second harmonic, the measured Q factor is approximately 1.6×10^4 [see Fig. 3(d)].

IV. SIMULATION AND DISCUSSION

To simulate the modes of fundamental and second-harmonic waves in the microresonator as shown in the inset of Fig. 1, a finite-element method is used without inclusion of the fiber taper [21]. The refractive indices used in the simulation are calculated using Sellmeier coefficients for congruently grown $LiNbO_3$ [22]. The ordinary indices are approximately 2.21 and approximately 2.26 at the fundamental and second-harmonic wavelengths, respectively. The extraordinary index is approximately 2.18 at the second-harmonic wavelength. For the TM modes, where the polarization is perpendicular to the optical axis of the crystal, the ordinary refractive index $n_o(\lambda)$ of bulk $LiNbO_3$ material is used. However, for the TE modes, the wave inevitably experiences the varying refractive index $n(\theta)$ along the periphery of the $LiNbO_3$ microresonator, which oscillates between the ordinary value $n_o(\lambda)$ and extraordinary value $n_e(\lambda)$ as below,

$$\frac{1}{n^2(\lambda,\theta)} = \frac{\cos^2\theta}{n_o^2(\lambda)} + \frac{\sin^2\theta}{n_e^2(\lambda)}. \quad (1)$$

In this case, an average refractive index can be obtained by integrating Eq. (1) with respect to the angle θ from 0 to 2π, which is given below,

$$n_{\mathrm{av}} = \left[\frac{1}{2}\left(\frac{1}{n_o^2(\lambda)} + \frac{1}{n_e^2(\lambda)}\right)\right]^{-1/2}. \quad (2)$$

This value is used as the refractive index of the bulk $LiNbO_3$ material to calculate the TE-polarized second-harmonic mode. All the geometrical parameters of the $LiNbO_3$ microdisk are chosen as that measured from the fabricated microdisk. By comparing our simulation results with the measured transmission spectrum in Fig. 3(a), the fundamental mode is identified to be a high-order mode of $TM_{6,359,1}$, where the subscript numbers (6,359,1) denote the radial-mode number, azimuthal-mode number, and axial-mode number, respectively. The second-harmonic mode is determined to be a high-order mode of $TE_{1,712,3}$, as shown in Fig. 3(b).

When the thin-film microresonator is considered as a 2D cavity for simplification, the refractive indices of bulk $LiNbO_3$ cannot be directly used and should be replaced by the effective refractive indices which depend on the geometry of the $LiNbO_3$ microresonator as well as mode spatial distributions. The effective refractive index n_F of the TM-polarized fundamental mode is calculated using the propagation constants of the WGMs [23]. The TE-polarized second-harmonic mode experiences a θ-dependent oscillation between the effective ordinary value n_o' and extraordinary value n_e' during circulating along the periphery. The effective ordinary (extraordinary) refractive index around wavelength of 770.065 nm can be estimated from the TE-polarization WGMs in a microresonator which has a geometry exactly the same as the $LiNbO_3$ microresonator used in our SHG experiment, however, with a constant ordinary (extraordinary) refractive index of the bulk $LiNbO_3$ crystal. Figure 4(a) shows the calculated effective refractive indices of the fundamental and second-harmonic modes (n_F and n_{SH}, respectively) as functions of azimuth angle θ. These two curves cross at the four azimuth angles of 0.591, 2.550, 3.733, and 5.692, where the phase mismatch between the fundamental and second-harmonic waves vanishes and the perfect phase-matching condition is fulfilled, as depicted in Fig. 4(b).

Similar to the effective refractive index of the second-harmonic wave, the nonlinear coefficient in the X-cut $LiNbO_3$ microresonator also varies cyclically with the azimuth angle, which is another determining factor in the SHG process. The second-order nonlinear coefficient along the periphery in the SHG process can be calculated by the equation [24]

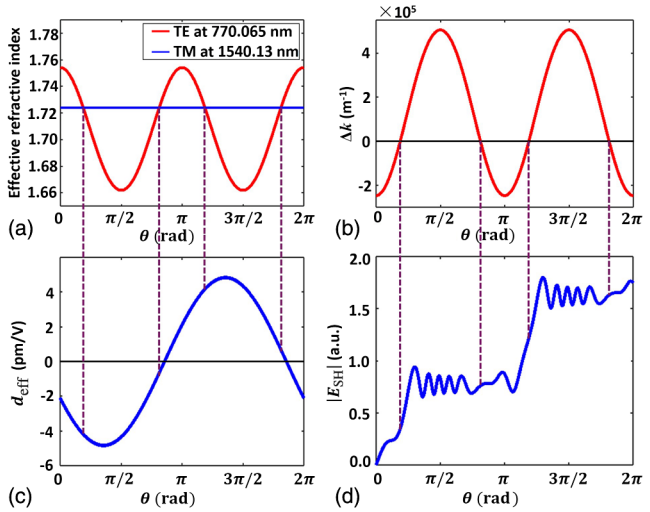

FIG. 4. Numerically calculated (a) effective refractive indices of the pump (solid blue curve) and second-harmonic modes (red dashed curve), (b) difference in the k vectors of the pump and second-harmonic modes (Δk), (c) nonlinear coefficient, and (d) electric field amplitude of the second-harmonic signal versus the azimuth angle along the microresonator periphery.

$$d_{\mathrm{eff}} = -d_{22}\cos\theta + d_{31}\sin\theta, \quad (3)$$

where d_{22} and d_{31} are the second-order nonlinear coefficients for the $LiNbO_3$ material. We assume $d_{22} = 2.1$ pm/V and $d_{31} = -4.35$ pm/V in this calculation [25]. Clearly, the effective nonlinear coefficient varies cyclically as a function of the azimuth angle θ. The calculated θ-dependent nonlinear coefficient is presented in Fig. 4(c). We find that among the four azimuth angles where the perfect phase matching is satisfied, the absolute values of the nonlinear coefficient at the angles $\theta = 0.591$ and $\theta = 3.733$ are much higher than those at the other two azimuth angles. Therefore, we expect that within one cycle, efficient growth of the second-harmonic signal will occur twice.

Finally, we calculate the field amplitude of the second-harmonic wave as it grows along the periphery of the microresonator. With undepleted pump approximation, we derive the equation that describes the growth of the second-harmonic field amplitude E_{SH} in the microresonator. We begin with the coupled-wave equations for sum-frequency generation [26]. Since we are discussing second-harmonic generation, a plane wave at the second-harmonic frequency ω_{SH} propagating in the $+s$ direction is

$$\tilde{E}_{\mathrm{SH}}(s,t) = E_{\mathrm{SH}}(s)e^{i\int k_{\mathrm{SH}}(s)ds - i\omega_{\mathrm{SH}}t} + \mathrm{c.c.}, \quad (4)$$

where $ds = R\cdot d\theta$, R is the radius of the microresonator, $k_{\mathrm{SH}}(s) = \frac{n_{\mathrm{SH}}(s)\omega_{\mathrm{SH}}}{c}$, $n_{\mathrm{SH}}^2 = \epsilon^{(1)}(\omega_{\mathrm{SH}})$, and c is the speed in vacuum. Based on the Maxwell equations, we have

$$\nabla^{(2)}\tilde{E}_{\mathrm{SH}} - \frac{\epsilon^{(1)}(\omega_{\mathrm{SH}})}{c^2}\frac{\partial^2\tilde{E}_{\mathrm{SH}}}{\partial t^2} = \frac{1}{\epsilon_0 c^2}\frac{\partial^2\tilde{P}_{\mathrm{SH}}}{\partial t^2}. \quad (5)$$

Here, $\tilde{P}_{\mathrm{SH}}$ is the second-order polarization, which appears as

$$\tilde{P}_{\mathrm{SH}}(s,t) = P_{\mathrm{SH}}e^{-i\omega_{\mathrm{SH}}t} + \mathrm{c.c.}, \quad (6)$$

where $P_{\mathrm{SH}} = 2\epsilon_0 d_{\mathrm{eff}}\tilde{E}_F^2(s)$, $\tilde{E}_F(s) = E_F e^{ik_F s} + \mathrm{c.c.}$, $k_F = 2\pi n_F/\lambda_F$, λ_F is the wavelength of the fundamental wave in vacuum, and E_F is the field amplitude of the fundamental wave circulated in the microresonator. Note that the overall conversion efficiency of our second-harmonic generation experiment is quite low (i.e., approximately 10^{-3}); therefore, the depletion of pump beam is neglected. In addition, with the plane-wave assumption, the second-harmonic field depends only on the coordinate s. Then we have

$$\nabla^{(2)}\tilde{E}_{\mathrm{SH}} = \left[\frac{d^2E_{\mathrm{SH}}}{ds^2} + 2ik_{\mathrm{SH}}\frac{dE_{\mathrm{SH}}}{ds} + iE_{\mathrm{SH}}\frac{dk_{\mathrm{SH}}}{ds} - k_{\mathrm{SH}}^2E_{\mathrm{SH}}\right] \times e^{i\int k_{\mathrm{SH}}ds - i\omega_{\mathrm{SH}}t} + \mathrm{c.c.} \quad (7)$$

We substitute Eqs. (4), (6), and (7) into the wave equation (5) and then obtain

$$\left[\frac{d^2E_{\mathrm{SH}}}{ds^2} + 2ik_{\mathrm{SH}}\frac{dE_{\mathrm{SH}}}{ds} + iE_{\mathrm{SH}}\frac{dk_{\mathrm{SH}}}{ds} - k_{\mathrm{SH}}^2E_{\mathrm{SH}} + \frac{\epsilon^{(1)}(\omega_{\mathrm{SH}})\omega_{\mathrm{SH}}^2}{c^2}E_{\mathrm{SH}}\right]e^{i\int k_{\mathrm{SH}}ds - i\omega_{\mathrm{SH}}t} + \mathrm{c.c.} = \frac{-2d_{\mathrm{eff}}\omega_{\mathrm{SH}}^2}{c^2}E_F^2e^{i(2k_Fs-\omega_{\mathrm{SH}}t)} + \mathrm{c.c.} \quad (8)$$

Since $k_{\mathrm{SH}}^2 = \frac{\epsilon^{(1)}(\omega_{\mathrm{SH}})\omega_{\mathrm{SH}}^2}{c^2}$, the fourth and fifth terms in the brackets of Eq. (8) cancel out. Equation (8) can be rewritten as

$$\frac{d^2E_{\mathrm{SH}}}{ds^2} + 2ik_{\mathrm{SH}}\frac{dE_{\mathrm{SH}}}{ds} + iE_{\mathrm{SH}}\frac{dk_{\mathrm{SH}}}{ds} = \frac{-2d_{\mathrm{eff}}\omega_{\mathrm{SH}}^2}{c^2}E_F^2e^{i(2k_Fs-\int k_{\mathrm{SH}}ds)}.$$

For the X-cut crystal microdisk, the pump wave has a constant k_F. We set $\Delta k = 2k_F - k_{\mathrm{SH}}$, and we obtain

$$\frac{d^2E_{\mathrm{SH}}}{ds^2} + 2ik_{\mathrm{SH}}\frac{dE_{\mathrm{SH}}}{ds} + iE_{\mathrm{SH}}\frac{dk_{\mathrm{SH}}}{ds} = \frac{-2d_{\mathrm{eff}}\omega_{\mathrm{SH}}^2}{c^2}E_F^2e^{i\int\Delta kds}. \quad (9)$$

Under the slowly varying amplitude approximation, namely, $|\frac{d^2E_{\mathrm{SH}}}{ds^2}| \ll |k_{\mathrm{SH}}\frac{dE_{\mathrm{SH}}}{ds}|$, Eq. (9) becomes

$$\frac{dE_{\mathrm{SH}}}{ds} = \frac{id_{\mathrm{eff}}\omega_{\mathrm{SH}}^2}{k_{\mathrm{SH}}c^2}E_F^2e^{i\int\Delta kds} - \frac{E_{\mathrm{SH}}}{2k_{\mathrm{SH}}}\times\frac{dk_{\mathrm{SH}}}{ds}. \quad (10)$$

The gain dynamics of SHG is investigated by integrating Eq. (10) along the periphery over a single cycle in the steady-state regime. Because of the periodic characteristic of the double-resonant SHG process, the calculation is carried out in the range of 0–2π for θ. Figure 4(d) shows how the second-harmonic field amplitude evolves in the microresonator as a function of the azimuth angle. It is observed that in the most angular range of θ where the phase matching is unavailable, the second-harmonic signal oscillates rapidly without significant gain. The oscillation is a clear indication of the periodic exchange of the energies between the fundamental and second-harmonic waves as a result of the phase mismatching. However, near the two azimuth angles $\theta = 0.591$ and $\theta = 3.733$ where the absolute value of the nonlinear coefficient is large and the perfect phase matching is fulfilled, the second-harmonic signal increases dramatically to facilitate the efficient SHG as observed in our experiment. This behavior provides the essential microscopic mechanism behind the result in Fig. 2(d). To estimate the conversion efficiency numerically, the fundamental light is assumed to be coupled into the microresonator in the critical coupling condition. Because of high-Q factor and small volume, the microresonator builds up a significant internal circulating field strength with low pump power [27]. The normalized conversion efficiency of SHG is calculated to be $4.03\times10^{-3}/\mathrm{mW}$ by integrating Eq. (10) using the parameters in our experiment. The calculation result is on the same order of magnitude as our experimental result, indicating a reasonable agreement between the theoretical and experimental results. We expect that extension of the CSPM mechanism to sub-100-μm crystalline microresonators can be effective for most negative uniaxial crystals. Additionally, we investigate other polarization cases (e.g., the fundamental wave is the TE mode, while second-harmonic wave is the TM mode), but the obtained conversion efficiency is lower than the result reported here because of poorer fulfillment of the double-resonance condition.

V. CONCLUSION

To conclude, we demonstrate highly efficient SHG in a high-Q $LiNbO_3$ microresonator fabricated by femtosecond-laser direct writing followed by FIB polishing. We perform efficient SHG with a normalized conversion efficiency of $1.106\times10^{-3}/\mathrm{mW}$, which is enabled by simultaneously fulfilling the phase matching and coherent double resonance. The approach will benefit ultra-low-threshold, efficient on-chip nonlinear wavelength conversion for modern classical and quantum-optical applications.

ACKNOWLEDGMENTS

The work is supported by National Basic Research Program of China (Grant No. 2014CB921300), NSFC (Grants No. 61275205, No. 11174305, No. 61405220, and No. 61505231), and the Fundamental Research Funds for the Central Universities.

[1] S. L. McCall, A. F. J. Levi, R. E. Slusher, S. J. Pearton, and R. A. Logan, Whispering-gallery mode microdisk lasers, Appl. Phys. Lett. **60**, 289 (1992).

[2] M. Kuwata-Gonokami, R. H. Jordan, A. Dodabalapur, H. E. Katz, M. L. Schilling, R. E. Slusher, and S. Ozawa, Polymer microdisk and microring lasers, Opt. Lett. **20**, 2093 (1995).

[3] D. K. Armani, T. J. Kippenberg, S. M. Spillane, and K. J. Vahala, Ultra-high-Q toroid microcavity on a chip, Nature (London) **421**, 925 (2003).

[4] K. J. Vahala, Optical microcavities, Nature (London) **424**, 839 (2003).

[5] L. He, Ş. K.Özdemir, J. Zhu, W. Kim, and L. Yang, Detecting single viruses and nanoparticles using whispering gallery microlasers, Nat. Nanotechnol. **6**, 428 (2011).

[6] A. A. Savchenkov, V. S. Ilchenko, A. B. Matsko, and L. Maleki, Kilohertz optical resonances in dielectric crystal cavities, Phys. Rev. A **70**, 051804(R) (2004).

[7] J. U. Fürst, D. V. Strekalov, D. Elser, M. Lassen, U. L. Andersen, C. Marquardt, and G. Leuchs, Naturally Phase-Matched Second-Harmonic Generation in a Whispering-Gallery-Mode Resonator, Phys. Rev. Lett. **104**, 153901 (2010).

[8] A. Guarino, G. Poberaj, D. Rezzonico, R. Degl'Innocenti, and P. Günter, Electro-optically tunable microring resonators in lithium niobate, Nat. Photonics **1**, 407 (2007).

[9] T.-J. Wang, J.-Y. He, C.-A. Lee, and H. Niu, High-quality $LiNbO_3$ microdisk resonators by undercut etching and surface tension reshaping, Opt. Express **20**, 28119 (2012).

[10] J. Lin, Y. Xu, Z. Fang, J. Song, N. Wang, L. Qiao, W. Fang, and Y. Cheng, Second harmonic generation in a high-Q lithium niobate microresonator fabricated by femtosecond laser micromachining, arXiv:1405.6473.

[11] J. Lin, Y. Xu, Z. Fang, M. Wang, J. Song, N. Wang, L. Qiao, W. Fang, and Y. Cheng, Fabrication of high-Q lithium niobate microresonators using femtosecond laser micromachining, Sci. Rep. **5**, 8072 (2015).

[12] C. Wang, M. J. Burek, Z. Lin, H. A. Atikian, V. Venkataraman, I.-C. Huang, P. Stark, and M. Lončar, Integrated high quality factor lithium niobate microdisk resonators, Opt. Express **22**, 30924 (2014).

[13] R. Wang and S. A. Bhave, Free-standing high quality factor thin-film lithium niobate micro-photonic disk, arXiv: 1409.6351.

[14] J. Lin, Y. Xu, J. Tang, N. Wang, J. Song, F. He, W. Fang, and Y. Cheng, Fabrication of three-dimensional microdisk resonators in calcium fluoride by femtosecond laser micromachining, Appl. Phys. A **116**, 2019 (2014).

[15] J. Wang, F. Bo, S. Wan, W. Li, F. Gao, J. Li, G. Zhang, and J. Xu, High-Q lithium niobate microdisk resonators on a chip for efficient electro-optic modulation, Opt. Express **23**, 23072 (2015).

[16] P. A. Franken, A. E. Hill, C. W. Peters, and G. Weinreich, Generation of Optical Harmonics, Phys. Rev. Lett. **7**, 118 (1961).

[17] P. D. Maker, R. W. Terhune, M. Nisenoff, and C. M. Savage, Effects of Dispersion and Focusing on the Production of Optical Harmonics, Phys. Rev. Lett. **8**, 21 (1962).

[18] J. A. Armstrong, N. Bloembergen, J. Ducuing, and P. S. Pershan, Interactions between light waves in a nonlinear dielectric, Phys. Rev. **127**, 1918 (1962).

[19] P. S. Kuo, J. Bravo-Abad, and G. S. Solomon, Second-harmonic generation using 4-quasi-phasematching in a GaAs whispering-gallery-mode microcavity, Nat. Commun. **5**, 3109 (2014).

[20] G. Lin, J. U. Fürst, D. V. Strekalov, and N. Yu, Wide-range cyclic phase matching and second harmonic generation in whispering gallery resonators, Appl. Phys. Lett. **103**, 181107 (2013).

[21] M. Oxborrow, Traceable 2-D finite-element simulation of the whispering-gallery modes of axisymmetric electromagnetic resonators, IEEE Trans. Microwave Theory Tech. **55**, 1209 (2007).

[22] D. E. Zelmon, D. L. Small, and D. Jundt, Infrared corrected Sellmeier coefficients for congruently grown lithium niobate and 5 mol.% magnesium oxide-doped lithium niobate, J. Opt. Soc. Am. B **14**, 3319 (1997).

[23] B. E. Little, J.-P. Laine, and H. A. Haus, Analytic theory of coupling from tapered fibers and half-blocks into microsphere resonator, J. Lightwave Technol. **17**, 704 (1999).

[24] B. E. A. Saleh and M. C. Teich, *Fundamentals of Photonics*, 2nd ed. (Wiley-Interscience, New York, 2007), pp. 873–936.

[25] V. G. Dmitriev, G. G. Gurzadyan, and D. N. Nikogosyan, *Handbook of Nonlinear Optical Crystals* (Springer-Verlag, Berlin, 1999), p. 125.

[26] R. W. Boyd, *Nonlinear Optics*, 3rd ed. (Academic Press, New York, 2008), pp. 69–79.

[27] H. Rokhsari and K. J. Vahala, Observation of Kerr nonlinearity in microcavities at room temperature, Opt. Lett. **30**, 427 (2005).